First-Principles Prediction of Potential Candidate Materials $M\mathrm{Cu_3}X_4$ (M = V, Nb, Ta; X = S, Se, Te) for Neuromorphic Computing

Baoxing Zhai,[1] Ruiqing Cheng,[1] Tianxing Wang,[2] Li Liu,[1] Lei Yin,[1] Yao Wen,[1] Hao Wang,[1] Sheng Chang,[1] and Jun He[1,3,*]

[1] *Key Laboratory of Artificial Micro- and Nano-structures of Ministry of Education, and School of Physics and Technology, Wuhan University, Wuhan 430072, China*

[2] *School of physics, Henan Normal University, Xinxiang 453007, China*

[3] *Wuhan Institute of Quantum Technology, Wuhan 430206, China*

(Received 15 November 2022; revised 27 March 2023; accepted 17 April 2023; published 12 May 2023)

Inspired by the neurosynaptic frameworks in the human brain, neuromorphic computing is expected to overcome the bottleneck of traditional von Neumann architecture and be used in artificial intelligence. Here, we predict a class of potential candidate materials, $M\mathrm{Cu_3}X_4$ (M = V, Nb, Ta; X = S, Se, Te), for neuromorphic computing applications through first-principles calculations based on density-functional theory. We find that when $M\mathrm{Cu_3}X_4$ are inserted with Li atom, the systems would transform from semiconductors to metals due to the considerable electron filling [approximately 0.8 electrons per formula unit (f.u.)] and still maintain well-structural stability. Meanwhile, the inserted Li atom also has a low diffusion barrier (approximately 0.6 eV/f.u.), which ensures the feasibility to control the insertion and extraction of Li by gate voltage. These results establish that the system can achieve the reversible switching between two stable memory states, i.e., high or low resistance state, indicating that it could potentially be used to design synaptic transistor to enable neuromorphic computing. Our work provides inspiration for advancing the search of candidate materials related to neuromorphic computing from the perspective of theoretical calculations.

DOI: 10.1103/PhysRevApplied.19.054045

I. INTRODUCTION

Industrial 4.0, also known as the era of intelligence, was put forward in 2014 [1], and artificial intelligence is expected to play an essential role in it. In recent years, many concepts have emerged around artificial intelligence, including neuromorphic computing [2–5], machine learning [6,7], and deep learning [8,9], etc. The research in these fields covers innovations in materials, electronic device structures, and program algorithms. For neuromorphic computing, it is considered to be an advanced brainlike computing method with the advantages of energy saving and high efficiency. At present, a variety of schemes have been proposed to realize neuromorphic computing, such as memristors [2,4], ion intercalation [10–13], structural phase transition [14–18], heterostructure engineering [19,20], and spintronic devices [21–24]. Among them, ionic synaptic transistors can be designed based on ion intercalation. As shown in Figs. 1(a) and 1(b), the structure of ionic synaptic transistors is basically the same as that of the traditional MOSFETs. The biggest difference is that ionic synaptic transistors replace the oxide insulating layer in MOSFETs with an electrolyte layer, allowing them to work differently. As shown in Fig. 1(c), when a positive gate voltage is applied, metal ions in the electrolyte layer of ionic synaptic transistors will enter the channel layer, causing a change in channel conductance. While in a MOSFET, the gate voltage is applied to regulate the movement of carriers. Taking the n-type semiconductor substrate as an example [Fig. 1(d)], when a positive gate voltage is applied, an electron accumulation layer will be formed in the channel. Moreover, after the gate voltage is removed, the MOSFET will immediately return to its original state, while for the ionic synaptic transistor, because the intercalated particles are retained in the channel layer, the regulated conductance can be maintained, i.e., nonvolatility. Zhu *et al.* [12] have experimentally demonstrated that the ionic synaptic transistors based on two-dimensional (2D) van der Waals materials possess excellent application prospect in neuromorphic computing. Their work shows that as metal ions have two diffusion modes in 2D layered materials, one is adsorbed on the surface of the material and the other is embedded in the material, the devices can generate both short-term and long-term signals [12]. However, the diffusion mode that across the layered materials themselves may induce structural distortions or defects,

*he-jun@whu.edu.cn

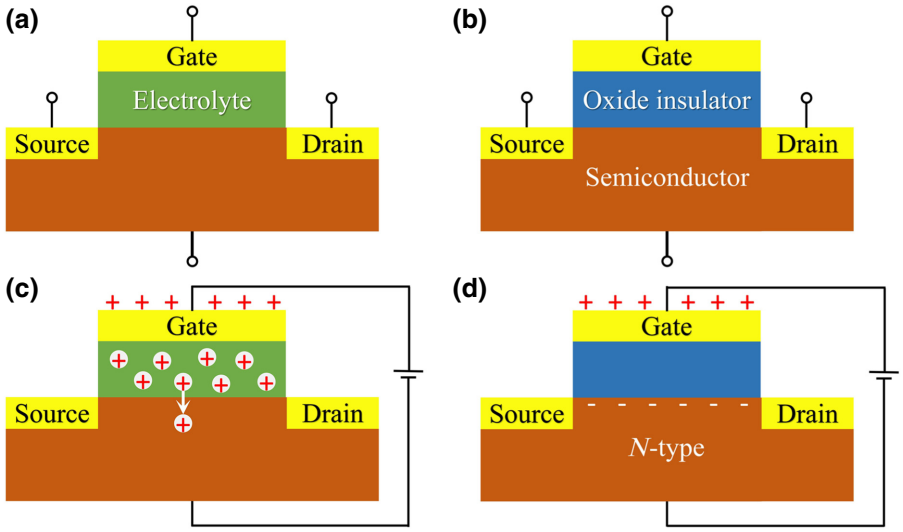

FIG. 1. Schematic diagram of the structures of (a) ionic synaptic transistors and (b) MOSFETs. Schematic diagram of the working principles of (c) ionic synaptic transistors and (d) MOSFETs.

which may challenge structural stability. Additionally, it has been reported that the structural transition of 2*H* phase and 1*T'* phase of MoS_2 can be realized by controlling the concentration of intercalated Li^+ ions [10]. These results undoubtedly add the uncertainty that synaptic transistors based on 2D layered materials may face in neuromorphic computing.

Nowadays, with the rapid improvement of computer computing power, people can quickly screen out abundant satisfactory materials with specific properties from the database by setting some indicators and conducting high-throughput search [25–27], which can greatly accelerate the development and application of new materials. Similarly, as the hardware carrier of neuromorphic computing, it is also vital to find and screen suitable materials for the development of neuromorphic computing. However, due to the diversity and complexity of current schemes for neuromorphic computing, it is still quite tough to screen and predict materials by high-throughput computing or machine-learning methods. In fact, to date, most materials studies related to neuromorphic computing are started from experiments, which undoubtedly limits the rapid development of the field.

Here, we note that MCu_3X_4 (M = V, Nb, Ta; X = S, Se, Te), a class of semiconductor materials with a cubic lattice, have $P\bar{4}3m$ symmetry [Figs. 2(a) and 2(b)]. Due to the suitable range of band gaps, these kinds of materials possess a great photoelectric application prospect [28–31]. In addition, they are theoretically predicted to have favorable thermoelectric properties [32,33]. We find that the structures of MCu_3X_4 have an intriguing feature, which is that there are no atoms in the body center and face center of their unit cells, just like an open framework. By contrast, fullerenes [34], a well-known class of carbon materials, are like a closed box. Numerous studies have shown that filling fullerenes with atoms may enable them to acquire some alternative physical properties [35–37]. As early as 1978, Arribart *et al.* [38] studied VCu_3S_4-embedded copper ions and pointed out that its crystal structure has the potential for intercalation research. Inspired by these studies and the above studies on neuromorphic computing, we speculate that MCu_3X_4 may be applied to neuromorphic computing by inserting atoms. However, until now, no one had done the research.

In this work, we explore the potential of MCu_3X_4 for neuromorphic computing through first-principles calculations. First, via structure optimization and transition-state search, we ascertain the crystal structure of the ground state with different inserted atoms (H/Li/Na/K) and the diffusion barrier of the inserted atoms. Then, the structural stability after inserting different atoms is compared by phonon spectra. By the above analysis, we confirm that Li atom is more suitable for inserting into MCu_3X_4. Subsequently, band-structure calculations and charge-transfer analysis show that the insertion of Li atom can transform MCu_3X_4 from semiconductors to metals due to the atomic insertion-induced electron filling. Finally, we quantitatively analyze the resistance ratio of VCu_3S_4 and Li-VCu_3S_4 via electrical transport simulation, which can reach a surprising magnitude of 10^{12}. These results signify that MCu_3X_4 meet the requirements of ionic synaptic transistors reported in Ref. [11], thus we believe that they have potential applications in the device related to neuromorphic computing.

II. COMPUTATIONAL METHODS

We perform first-principles calculations implemented in the Vienna *ab initio* simulation package (VASP) based on density-functional theory (DFT) [39]. The exchange

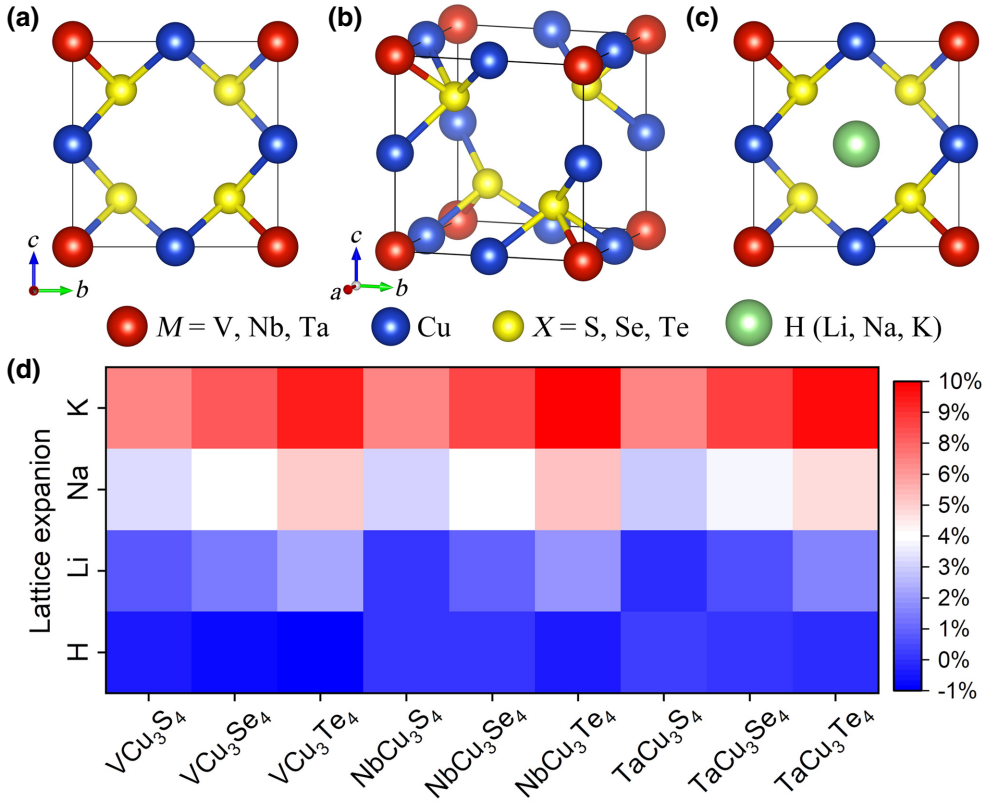

FIG. 2. (a) Side view of the MCu_3X_4 unit cell alone the a axis, the same as that along the b and c axes. (b) three-dimensional structural view of the MCu_3X_4 unit cell. (c) Schematic diagram of inserting the atom at the central site of the MCu_3X_4 unit cell. (d) Calculated lattice expanion rates induced by inserting different atoms in MCu_3X_4.

correlation potential is described with the Perdew-Burke-Ernzerhof (PBE) of the generalized gradient approximation (GGA) [40]. The PBE + U based on the approach of Dudarev *et al.* [41] is adopted for Cu 3d electrons with $U = 5.2$ eV [28]. The electron-ion potential is described by the projected augmented wave (PAW) [42]. The kinetic energy cutoff of the plane wave is set to be 500 eV for the plane-wave expansion. The Brillouin-zone integration is carried out using $5 \times 5 \times 5$ Monkhorst-Pack k-point meshes for geometry optimization of MCu_3X_4 [43]. All geometric structures are fully relaxed until energy and forces are converged to 10^{-6} eV and 0.01 eV/Å, respectively.

We study the transport properties of MCu_3X_4-based ionic synaptic transistors using the Atomistix Toolkit-Virtual Nanolab (ATK-VNL) 2017 package with DFT and nonequilibrium Green function methods [44,45]. The electron exchange correlation is treated by GGA PBE the same as the calculation in VASP. The structural relaxations of each device system are performed in advance and allowed until the absolute value of force acting on each atom is less than 0.05 eV/Å. The mesh cutoff is set as 75 Hartree, and the k-point grid $11 \times 11 \times 101$ is used to sample the Brillouin zone of the electrodes in the x, y, and z (transport direction) directions, respectively. The temperature of electrodes is set to 300 K to accelerate the transport calculation.

The nonequilibrium electron transport currents of state 1 [Fig. 8(b)] at finite bias voltages are calculated by the Landauer-Buttiker formula:

$$I = \frac{e}{h}\int_{-\infty}^{\infty}\{T(E,V_b)[f_L(E-\mu_L) - f_R(E-\mu_R)]\}dE,$$

where $T(E, V_b)$ is the transmission coefficient under a finite bias V_b, $f_{L/R}(E-\mu_{L/R})$ corresponding to the Fermi-Dirac distribution for the left and right electrode, and $\mu_{L/R} = E_F \pm (1/2)eV_b$ represents the electrochemical potential of the left and right electrode. The I-V curve of state 2 [Fig. 8(b)] is calculated by integrating the zero-bias transmission spectrum in an increasingly wide bias interval.

III. RESULTS AND DISCUSSIONS

The calculated geometric parameters (Table I) and band structures (Fig. S1 within the Supplemental Material [46]) of MCu_3X_4 are in accordance with a previous report [28]. We herein try four kinds of atoms H/Li/Na/K, and select the center of the unit cell as an insertion site, as shown in Fig. 2(c). The results show that inserting the atom at the

TABLE I. Calculated lattice constants for isolated $MCu_3X_4(a)$ and inserting H(a_H), Li(a_{Li}), Na(a_{Na}), and K(a_K) atoms into MCu_3X_4, and band gap E_g of MCu_3X_4 using the PBE method. The lattice constants in parentheses are obtained by the PBE + U method.

Compound	a (Å)	a_H (Å)	a_{Li} (Å)	a_{Na} (Å)	a_K (Å)	E_g (eV)
VCu_3S_4	5.437 (5.464)	5.421	5.487 (5.512)	5.631	5.815	1.141
VCu_3Se_4	5.649 (5.675)	5.609	5.742 (5.762)	5.896	6.092	0.887
VCu_3Te_4	5.954 (5.983)	5.905	6.108 (6.129)	6.285	6.490	0.579
$NbCu_3S_4$	5.540 (5.579)	5.550	5.557 (5.572)	5.726	5.925	1.905
$NbCu_3Se_4$	5.726 (5.749)	5.735	5.791 (5.816)	5.975	6.190	1.505
$NbCu_3Te_4$	6.013 (6.049)	6.001	6.147 (6.171)	6.351	6.592	1.030
$TaCu_3S_4$	5.552 (5.586)	5.574	5.555 (5.575)	5.731	5.938	2.194
$TaCu_3Se_4$	5.725 (5.791)	5.736	5.771 (5.804)	5.963	6.198	1.820
$TaCu_3Te_4$	6.020 (6.054)	6.020	6.133 (6.167)	6.331	6.585	1.242

central site does not alter the lattice type and symmetry of MCu_3X_4, except for the lattice constants, see Table I. Figure 2(d) plots the lattice expansion rates of MCu_3X_4 after inserting different atoms, which is obtained by the formula $\eta = (a_1 - a_0)/a_0$, where a_0 are the original lattice constants of MCu_3X_4, and a_1 are the lattice constants after inserting the atom. It can be seen that the lattice expansion rate will gradually rise with the atomic radius of the inserted atom.

To evaluate the effect of inserted atom on the structural stability of MCu_3X_4, we first perform a transition-state search using the climbing-image nudged-elastic-band method [47] to determine whether the central site is the lowest energy site of the inserted atom. The simulated diffusion process of the inserted atom in MCu_3X_4 is shown within the Supplemental Material [46], and the calculated diffusion barrier is plotted in Fig. 3. The following two rules are found: (i) For the same material, the diffusion barrier aggrandizes gradually with the increase of the mass and radius of the inserted atom (H < Li < Na < K). (ii) For the same inserted atom, the increase of atomic mass and radius of X atom (S < Se < Te) will also augment the diffusion barrier. Among them, the second rule is somewhat unexpected, because normally, the lattice constant of MCu_3X_4 increases with the radius of the X atom, thus increasing the channel size and making the inserted atom easier to diffuse. We herein propose an explanation. As shown in Fig. 4, we use d_{X-X} to represent the distance between two X atoms and find that d_{X-X} does increase with the atomic number of X (Table II), but meanwhile, the

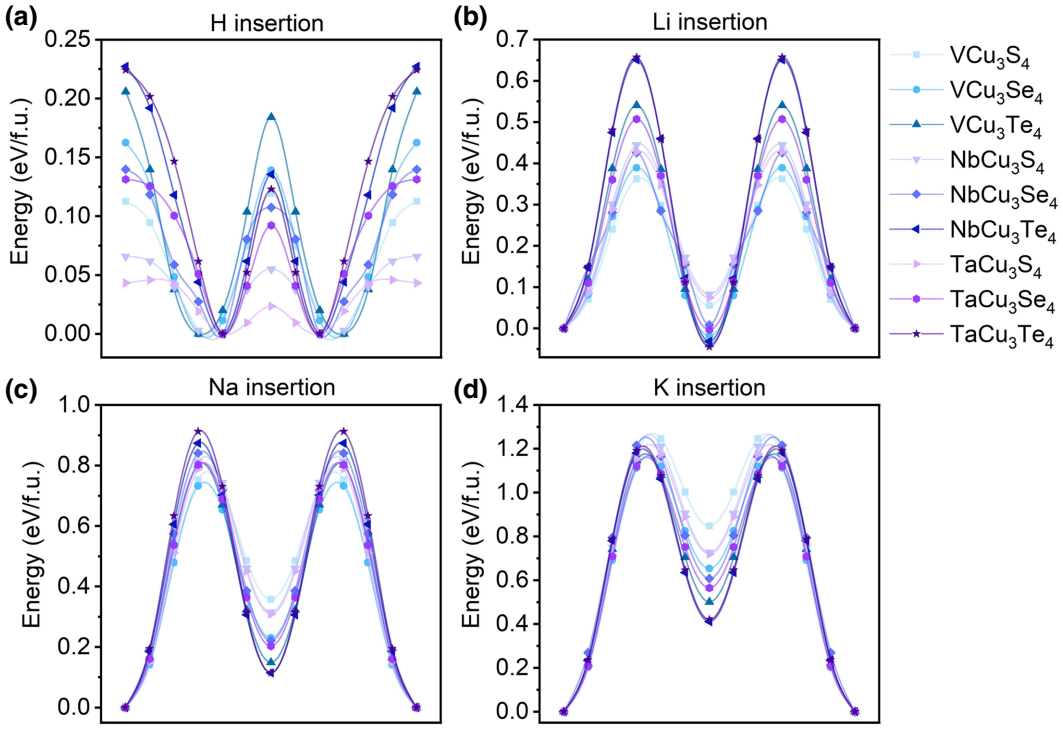

FIG. 3. Diffusion barriers of the inserted atoms (H/Li/Na/K) in MCu_3X_4.

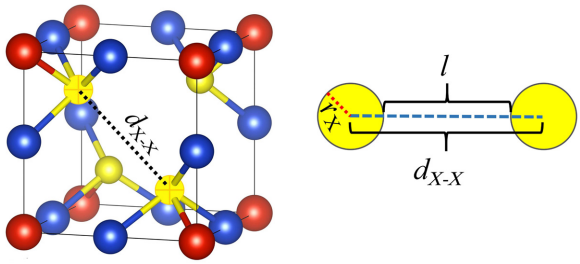

FIG. 4. Crystal structure of $M\mathrm{Cu_3}X_4$ unit cell. d_{X-X} is the distance between X atom and X atom, and r_X is the radius of X atom. The atomic radii of S, Se, and Te are 1.09, 1.22, and 1.42 Å, respectively.

atomic radius of X also increases. We set $l = d_{X-X} - 2r_X$ and measure the channel size by l. As shown in Table II, l decreases with the increase of the atomic number of X, indicating that the increase of r_X cancels out the increase of d_{X-X}, which adds the probability of the electron cloud overlapping between the inserted atom and the X atom, thus enhancing the interaction between them. As a result, the diffusion barrier of the inserted atom in $M\mathrm{Cu_3}X_4$ increases with the atomic number of X.

We also find that the lowest energy site for inserting the H atom is not the central site as shown in Fig. 2(c). The results of structure reoptimization show that H-$M\mathrm{Cu_3}X_4$ will transform into monoclinic crystal when the inserted H atom is located at the lowest energy site, see Fig. S3 within the Supplemental Material [46]. While for the inserted Li/Na/K atom, there is a transition state, which is the face-center position of the $M\mathrm{Cu_3}X_4$ unit cell. As the inserted atomic radius enlarges, the energy difference between the transition state and the ground state gradually increases, whilst for Li-$M\mathrm{Cu_3Te_4}$, the energy of the transition state is lower than that of the initial structure.

We subsequently calculate the phonon spectra of $M\mathrm{Cu_3}X_4$ after filling atoms, see Fig. 5 and Fig. S4 within the Supplemental Material [46]. For the H atom insertion, the structure in Fig. S3 within the Supplemental Material [46] is used. The results show that when inserting the H atom, there is still a deep imaginary frequency in the phonon spectra even for the H atom locating at the lowest energy position, suggesting that H-$M\mathrm{Cu_3}X_4$ have dynamic instability. While for the insertion of the Li/Na/K atom, the structure is adopted as shown in Fig. 2(c), and the stability of which would decline as the atomic radius and mass of the Li/Na/K atom rise. Since the Li atom has the proper atomic radius and mass, the phonon spectra of all Li insertion structures have no imaginary frequency, demonstrating that Li-$M\mathrm{Cu_3}X_4$ have favorable dynamic stability, while K-$M\mathrm{Cu_3}X_4$ have the opposite. Thus, we conclude that for H/Li/Na/K insertion $M\mathrm{Cu_3}X_4$, Li-$M\mathrm{Cu_3S_4}$ may be the best choice as it has relatively low diffusion barrier while ensuring structural stability.

We now confirm that inserting the Li atom into $M\mathrm{Cu_3}X_4$ can still maintain excellent structural stability, which meets the requirements of nonvolatile and long cycle life of basic device units for neuromorphic computing. However, there is another requirement: two vastly different resistance states before and after inserting the Li atom. Hence, the band structures of Li-$M\mathrm{Cu_3}X_4$ are calculated as shown in Fig. 6(a) and Fig. S(5) within the Supplemental Material [46], which shows that Li-$M\mathrm{Cu_3}X_4$ all possess the band characteristics of metal with the Fermi level across the conduction band, meaning that the insertion of the Li atom transforms $M\mathrm{Cu_3}X_4$ from semiconductors to metals. Moreover, the insertion of Li atom has nearly no effect on the band dispersion of $M\mathrm{Cu_3}X_4$, but only raises the position of the Fermi level, which is similar to the band regulation achieved by electron doping [48]. We next verify the above inference by Bader charge analysis [49], which shows that 0.8–0.86 electrons per f.u. are transferred from Li to $M\mathrm{Cu_3}X_4$, see Fig. S(6) within the Supplemental Material [46], and it is this high concentration of electron doping that makes $M\mathrm{Cu_3}X_4$ transform from semiconductors to metals. Recently, controllable hydrogenation accompanied by electron filling to achieve a tunable insulator-metal transition in $\mathrm{VO_2}$ was reported [50], which provides strong support for our above analysis.

Additionally, we find that for the V, Nb, and Ta elements, the V element compounds usually use the PBE + U method to study the electronic structures [51]. Therefore, to confirm the influence of PBE + U for the V atom on the results calculated in this work, we decide to take $\mathrm{VCu_3S_4}$ as an example for testing. As shown in Fig. 7, after considering PBE + U for the V atom, the band dispersion of $\mathrm{VCu_3S_4}$ hardly changes, only the band gap increases, while Li-$\mathrm{VCu_3S_4}$ still has the band characteristic of metal but shows the more obvious spin splitting. Thus, we know that although PBE + U for the V atom will have an effect on the electronic structure of $\mathrm{VCu_3S_4}$(Li-$\mathrm{VCu_3S_4}$), it will not change the main conclusion of this paper, namely, the Li atom insertion will cause the transition of $\mathrm{VCu_3S_4}$ from semiconductor to metal.

TABLE II. Calculated d_{X-X} and l in Fig. 4.

Compound	$\mathrm{VCu_3S_4}$	$\mathrm{VCu_3Se_4}$	$\mathrm{VCu_3Te_4}$	$\mathrm{NbCu_3S_4}$	$\mathrm{NbCu_3Se_4}$	$\mathrm{NbCu_3Te_4}$	$\mathrm{TaCu_3S_4}$	$\mathrm{TaCu_3Se_4}$	$\mathrm{TaCu_3Te_4}$
d_{X-X} (Å)	4.067	4.123	4.204	4.048	4.063	4.147	4.063	4.065	4.160
l (Å)	1.887	1.683	1.364	1.868	1.623	1.307	1.883	1.625	1.320

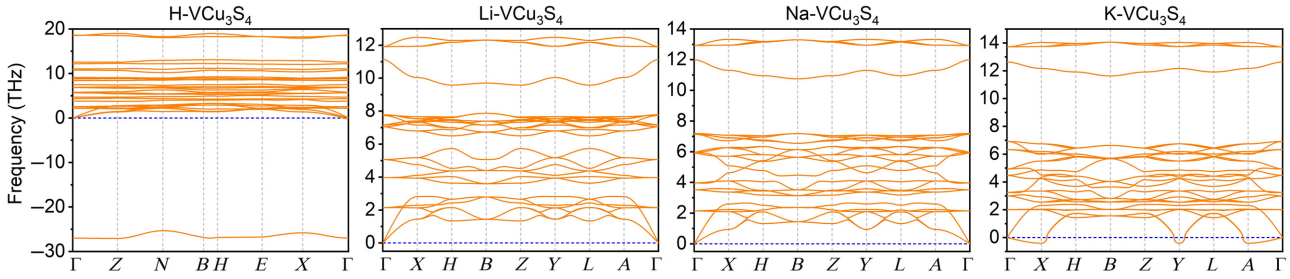

FIG. 5. Several representative phonon spectra of $M\mathrm{Cu}_3X_4$ with inserting different atoms.

Remarkably, Li-VCu_3X_4 and Li-NbCu_3X_4 appear spin polarization with a $1\mu_B$/f.u. and $0.25\mu_B$/f.u. average magnetic moment, respectively. Due to the obvious spin splitting (approximately 0.8 eV) in the band of Li-VCu_3X_4, it has the band characteristics of half-metal [48,52], that is, only the spin-up bands cross the Fermi level. From the density of states in Fig. 6(b), the conduction band of Li-$M\mathrm{Cu}_3X_4$ near the Fermi level is mainly contributed by M-d states, and the degree of spin polarization of M-d states gradually vanishes from left to right, corresponding to the change of magnetic moment, indicating that the magnetism originates from M-d states. For this, we attribute it to the M valence transition caused by electron filling accompanying with the insertion of Li atom.

For isolated $M\mathrm{Cu}_3X_4$, X is the sixth main family element, usually -2 valence in compounds; the valence electron of Cu is $3d^{10}4s^1$, and that of M is $3d^34s^2$, $4d^45s^1$, and $5d^36s^2$ for V, Nb and Ta, respectively. Therefore, we infer that the valence of M, Cu, and X for $M\mathrm{Cu}_3X_4$ are, respectively, $+5$, $+1$, and -2 according to charge conservation, so there is no lone pair electron and consequently no magnetism in $M\mathrm{Cu}_3X_4$. While Li atom is inserted into $M\mathrm{Cu}_3X_4$, $\mathrm{Li}^{+1}[M\mathrm{Cu}_3X_4]^{-1}$ would be formed. From the charge transfer in Fig. S(6) within the Supplemental Material [46], it can be seen that the electrons of Li are mainly transferred to X, while for X^{2-}, the outermost electron orbital is already full, and thus the electrons from Li cannot be stably bound and may be acquired by M. The probability of M acquiring these electrons can be estimated according to the following ionicity formula defined by the Paling, $f_i = 1 - \exp[-(x_A - x_B)^2/4]$, where x_A and x_B represent the electronegativity of atom A and atom B, respectively. V/Nb/Ta is the fifth subgroup element, the electronegativity of which weakens with the increase of their atomic

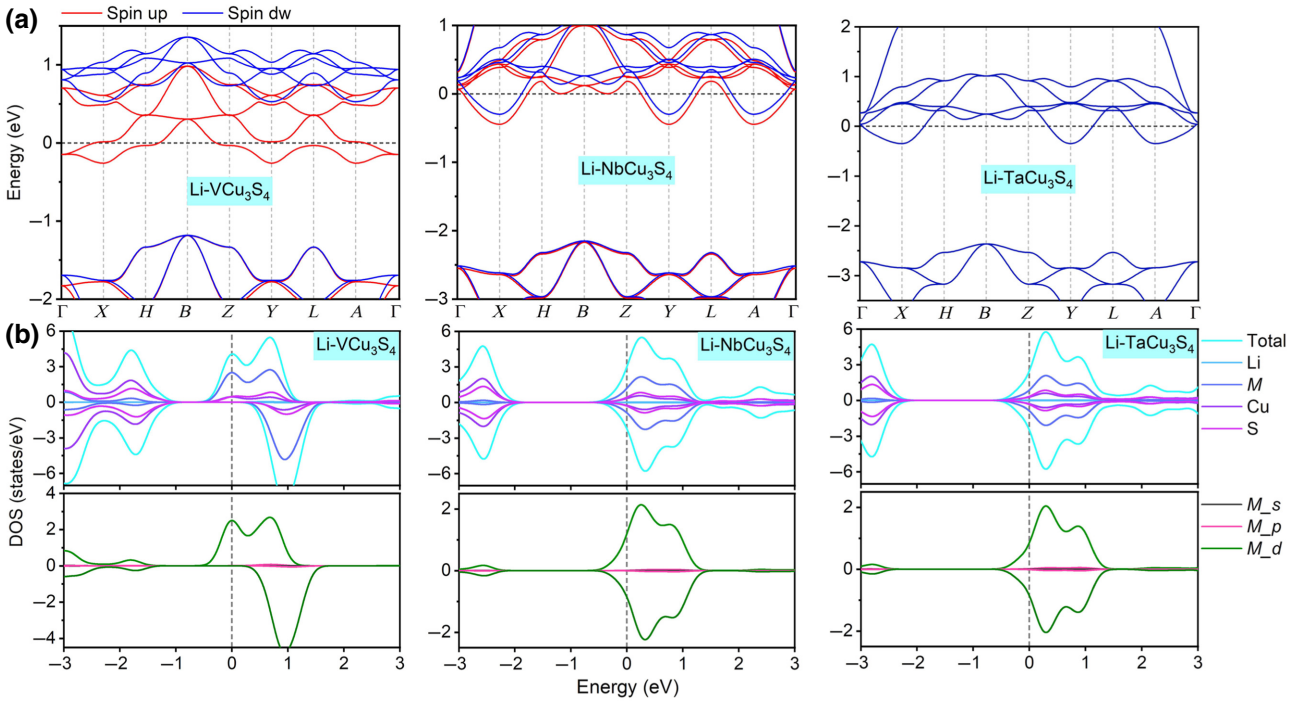

FIG. 6. (a) Band structures of Li-$M\mathrm{Cu}_3\mathrm{S}_4$. (b) Projected density of states of Li-$M\mathrm{Cu}_3\mathrm{S}_4$.

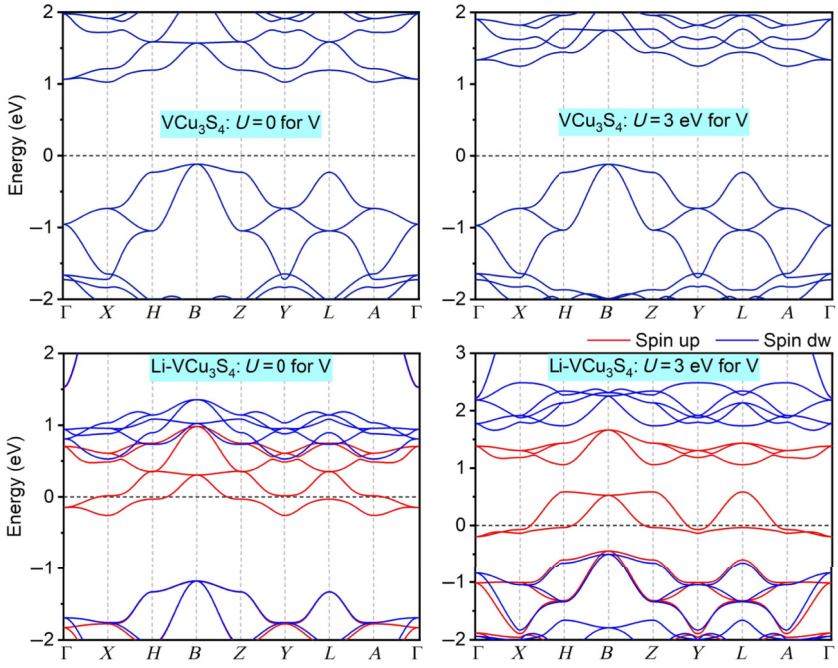

FIG. 7. Calculated band structures of VCu_3S_4 and Li-VCu_3S_4 with and without the PBE + U method for V 3d states.

number, corresponding to the enhanced ionicity between M and X. The stronger ionicity, the harder it is to transfer electrons from X to M. Thus for V/Nb/Ta, V atom gains the most electrons from X and possibly changes from V^{5+} to V^{4+}, resulting in a $1\mu_B$/f.u. magnetic moment; Nb atom gets fewer electrons from X and thus has a smaller magnetic moment; Ta atom recovers almost no electrons from X, so there is no spin polarization. In addition, we also compare the energy of ferromagnetic order and antiferromagnetic order of Li-VCu_3X_4 and confirm that the ferromagnetic state is the energy ground state, see Fig. S7 and Table S2 within the Supplemental Material [46].

Through the above research, we basically confirm that MCu_3X_4 can be used to design ion synaptic transistors. The

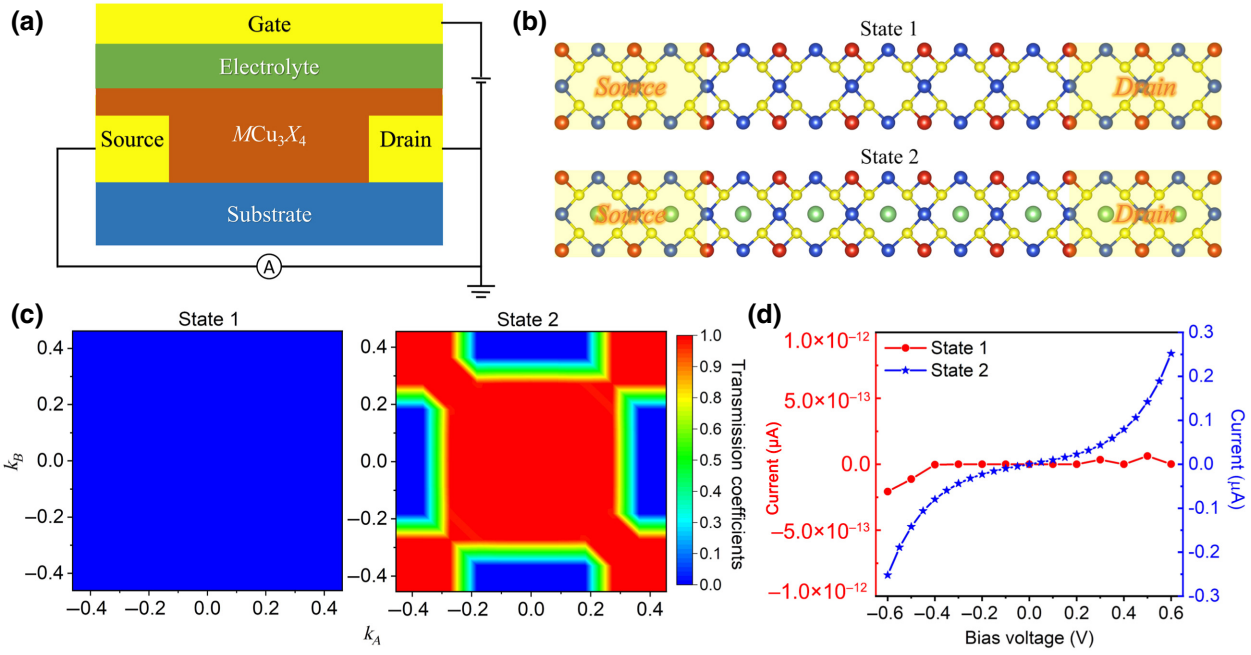

FIG. 8. (a) Schematic of the ionic synaptic transistor based on MCu_3X_4. (b) Two ideal states of the device as shown in (a) are realized by adjusting the lithium atoms embedding and stripping through the gate voltage. (c) Calculated zero-bias transmission coefficients at the Fermi level of device states 1 and 2 as shown in (b). (d) Calculated I-V curves of device states 1 and 2 as shown in (b).

device model is shown in Fig. 8(a), and its working principle is the same as that in Ref. [11]. To further evaluate the device performance, we take VCu_3S_4 as an example and quantitatively analyze the electrical transport properties of the device. Figure 8(b) shows two ideal states of the device, which can be achieved by controlling Li insertion and extraction. The transmission coefficient can represent the probability of a particle tunneling through a barrier. Figure 8(c) plots the zero-bias transmission coefficients of state 1 and state 2 at the Fermi level, which are close to 0 and 1 for state 1 and state 2, respectively, corresponding to the semiconducting feature of VCu_3S_4 and metallic feature of Li-VCu_3S_4. We next plot the volt-ampere characteristic curves of state 1 and state 2 in Fig. 8(d). The results show that under the same bias range (−0.6 to 0.6 V), the current of state 1 is in the order of 10^{-13} μA, while that of state 2 is in the order of 0.1 μA, indicating that the resistance ratio of two states reaches a surprising order of 10^{12}. Finally, we also consider the electron structures of the partial filling states for inserting Li into VCu_3S_4. The results show that VCu_3S_4 can achieve the semiconductor-metal transition at a lower inserted Li concentration (0.46%–1.54%), see the Supplemental Material [46].

IV. SUMMARY AND DISSCUSSION

In summary, we propose a promising class of candidate materials MCu_3X_4 for neuromorphic computing through first-principles simulations. When Li atom is inserted into MCu_3X_4 to form Li-MCu_3X_4, it not only maintains good structural stability, but also transforms from semiconductors to metals. Meanwhile, the low diffusion barrier of Li atom in MCu_3X_4 ensures the feasibility of gated Li insertion and extraction. These results show that MCu_3X_4 can be used to design ionic synaptic transistors and provide inspiration for the search of candidate materials related to neuromorphic computing by theoretical calculations. It is believed that with the upgrading of computers and algorithms, self-optimization and upgrading of artificial intelligence with autonomous learning ability based on neuromorphic computing will become a reality in the future. Last but not least, there are still some details of this work that deserve further investigation. For example, Li-VCu_3X_4 with half-metallicity may have potential applications in spintronic devices and whether Li-MCu_3X_4 may be used in solid-state ion batteries [53].

ACKNOWLEDGMENTS

This work is supported by National Key R&D Program of China (Grant No. 2018YFA0703700), the National Natural Science Foundation of China (Grants No. 91964203, No. 62274121, No. 62104171, No. 62104172, and No. 62004142), the Strategic Priority Research Program of Chinese Academy of Sciences (Grant No. XDB44000000), the Natural Science Foundation of Hubei Province, China (Grant No. 2021CFB037), and the Fundamental Research Funds for the Central Universities (Grant No. 2042021kf0067). The numerical calculations in this paper are performed on the supercomputing system in the Supercomputing Center of Wuhan University.

[1] H. Lasi, P. Fettke, H.-G. Kemper, T. Feld, and M. Hoffmann, Industry 4.0, Bus. Inf. Syst. Eng. **6**, 239 (2014).
[2] S. H. Jo, T. Chang, I. Ebong, B. B. Bhadviya, P. Mazumder, and W. Lu, Nanoscale memristor device as synapse in neuromorphic systems, Nano Lett. **10**, 1297 (2010).
[3] J. J. Yang, D. B. Strukov, and D. R. Stewart, Memristive devices for computing, Nat. Nanotechnol. **8**, 13 (2013).
[4] Z. Wang, S. Joshi, S. E. Savel'ev, H. Jiang, R. Midya, P. Lin, M. Hu, N. Ge, J. P. Strachan, Z. Li, *et al.*, Memristors with diffusive dynamics as synaptic emulators for neuromorphic computing, Nat. Mater. **16**, 101 (2017).
[5] Y. van de Burgt, E. Lubberman, E. J. Fuller, S. T. Keene, G. C. Faria, S. Agarwal, M. J. Marinella, A. Alec Talin, and A. Salleo, A non-volatile organic electrochemical device as a low-voltage artificial synapse for neuromorphic computing, Nat. Mater. **16**, 414 (2017).
[6] C. Cortes and V. Vapnik, Support-vector networks, Mach. Learn. **20**, 273 (1995).
[7] F. Pedregosa, G. Varoquaux, A. Gramfort, V. Michel, B. Thirion, O. Grisel, M. Blondel, P. Prettenhofer, R. Weiss, V. Dubourg, *et al.*, Scikit-Learn: Machine learning in Python, J. Mach. Learn. Res. **12**, 2825 (2011).
[8] Y. LeCun, Y. Bengio, and G. Hinton, Deep learning, Nature **521**, 436 (2015).
[9] V. Mnih, K. Kavukcuoglu, D. Silver, A. A. Rusu, J. Veness, M. G. Bellemare, A. Graves, M. Riedmiller, A. K. Fidjeland, G. Ostrovski, *et al.*, Human-level control through deep reinforcement learning, Nature **518**, 529 (2015).
[10] X. Zhu, D. Li, X. Liang, and W. D. Lu, Ionic modulation and ionic coupling effects in MoS_2 devices for neuromorphic computing, Nat. Mater. **18**, 141 (2019).
[11] E. J. Fuller, F. E. Gabaly, F. Léonard, S. Agarwal, S. J. Plimpton, R. B. Jacobs-Gedrim, C. D. James, M. J. Marinella, and A. A. Talin, Li-ion synaptic transistor for low power analog computing, Adv. Mater. **29**, 1604310 (2017).
[12] J. Zhu, Y. Yang, R. Jia, Z. Liang, W. Zhu, Z. U. Rehman, L. Bao, X. Zhang, Y. Cai, L. Song, *et al.*, Ion gated synaptic transistors based on 2D van der Waals crystals with tunable diffusive dynamics, Adv. Mater. **30**, 1800195 (2018).
[13] D. Kireev, S. Liu, H. Jin, T. Patrick Xiao, C. H. Bennett, D. Akinwande, and J. A. C. Incorvia, Metaplastic and energy-efficient biocompatible graphene artificial synaptic transistors for enhanced accuracy neuromorphic computing, Nat. Commun. **13**, 4386 (2022).
[14] B. Zhao and J. Ravichandran, Low-Power Microwave Relaxation Oscillators Based on Phase-Change Oxides for Neuromorphic Computing, Phys. Rev. Appl. **11**, 014020 (2019).
[15] Y. Shi and L.-Q. Chen, Intrinsic Insulator-Metal Phase Oscillations, Phys. Rev. Appl. **17**, 014042 (2022).

[16] C. Adda, M.-H. Lee, Y. Kalcheim, P. Salev, R. Rocco, N. M. Vargas, N. Ghazikhanian, C.-P. Li, G. Albright, M. Rozenberg, *et al.*, Direct Observation of the Electrically Triggered Insulator-Metal Transition in V_3O_5 Far below the Transition Temperature, Phys. Rev. X **12**, 011025 (2022).

[17] G. Li, D. Xie, H. Zhong, Z. Zhang, X. Fu, Q. Zhou, Q. Li, H. Ni, J. Wang, E. Guo, *et al.*, Photo-induced non-volatile VO_2 phase transition for neuromorphic ultraviolet sensors, Nat. Commun. **13**, 1729 (2022).

[18] M. S. Nikoo, R. Soleimanzadeh, A. Krammer, G. M. Marega, Y. Park, J. Son, A. Schueler, A. Kis, P. J. W. Moll, and E. Matioli, Electrical control of glass-like dynamics in vanadium dioxide for data storage and processing, Nat. Electron. **5**, 596 (2022).

[19] L. Xu, H. Xiong, Z. Fu, M. Deng, S. Wang, J. Zhang, L. Shang, K. Jiang, Y. Li, L. Zhu, *et al.*, High Conductance Margin for Efficient Neuromorphic Computing Enabled by Stacking Nonvolatile van der Waals Transistors, Phys. Rev. Appl. **16**, 044049 (2021).

[20] Y. Wang, W. Li, Y. Guo, X. Huang, Z. Luo, S. Wu, H. Wang, J. Chen, X. Li, X. Zhan, *et al.*, A gate-tunable artificial synapse based on vertically assembled van der Waals ferroelectric heterojunction, J. Mater. Sci. Technol. **128**, 239 (2022).

[21] D. Prychynenko, M. Sitte, K. Litzius, B. Krüger, G. Bourianoff, M. Kläui, J. Sinova, and K. Everschor-Sitte, Magnetic Skyrmion as a Nonlinear Resistive Element: A Potential Building Block for Reservoir Computing, Phys. Rev. Appl. **9**, 014034 (2018).

[22] R. Chen, C. Li, Y. Li, J. J. Miles, G. Indiveri, S. Furber, V. F. Pavlidis, and C. Moutafis, Nanoscale Room-Temperature Multilayer Skyrmionic Synapse for Deep Spiking Neural Networks, Phys. Rev. Appl. **14**, 014096 (2020).

[23] S. Zhang and Y. Tserkovnyak, Antiferromagnet-Based Neuromorphics Using Dynamics of Topological Charges, Phys. Rev. Lett. **125**, 207202 (2020).

[24] D. Marković, M. W. Daniels, P. Sethi, A. D. Kent, M. D. Stiles, and J. Grollier, Easy-plane spin Hall nano-oscillators as spiking neurons for neuromorphic computing, Phys. Rev. B **105**, 014411 (2022).

[25] M. G. Vergniory, L. Elcoro, C. Felser, N. Regnault, B. A. Bernevig, and Z. Wang, A complete catalogue of high-quality topological materials, Nature **566**, 480 (2019).

[26] Y. Xu, L. Elcoro, Z.-D. Song, B. J. Wieder, M. G. Vergniory, N. Regnault, Y. Chen, C. Felser, and B. A. Bernevig, High-throughput calculations of magnetic topological materials, Nature **586**, 702 (2020).

[27] N. Regnault, Y. Xu, M.-R. Li, D.-S. Ma, M. Jovanovic, A. Yazdani, S. S. P. Parkin, C. Felser, L. M. Schoop, N. Phuan Ong, *et al.*, Catalogue of flat-band stoichiometric materials, Nature **603**, 824 (2022).

[28] A. B. Kehoe, The electronic structure of sulvanite structured semiconductors Cu_3MCh_4(M = V, Nb, Ta; Ch = S, Se, Te): Prospects for optoelectronic applications, J. Mater. Chem. C **3**, 12236 (2015).

[29] Y. Li, M. Wu, T. Zhang, X. Qi, G. Ming, G. Wang, X. Quan, and D. Yang, Natural sulvanite Cu_3MX_4 (M = Nb, Ta; X = S, Se): Promising visible-light photocatalysts for water splitting, Comput. Mater. Sci. **165**, 137 (2019).

[30] V. Mantella, S. Ninova, S. Saris, A. Loiudice, U. Aschauer, and R. Buonsanti, Synthesis and size-dependent optical properties of intermediate band gap Cu_3VS_4 nanocrystals, Chem. Mater. **31**, 532 (2019).

[31] M. Liu, C.-Y. Lai, G. S. Selopal, and D. R. Radu, Synthesis and optoelectronic properties of Cu_3VSe_4 nanocrystals, PLoS One **15**, e0232184 (2020).

[32] E. Haque, Outstanding thermoelectric performance of MCu_3X_4 (M = V, Nb, Ta; X = S, Se, Te) with unaffected band degeneracy under pressure, ACS Appl. Energy Mater. **4**, 1942 (2021).

[33] J. Wen, H. Huang, X. Yu, D. Wang, K. Guo, D. Wan, J. Luo, and J.-T. Zhao, Thermoelectric properties of p-type Cu_3VSe_4 with high Seebeck coefficients, J. Alloys Compd. **879**, 160387 (2021).

[34] H. W. Kroto, The stability of the fullerenes C_n, with $n = 24$, 28, 32, 36, 50, 60 and 70, Nature **329**, 529 (1987).

[35] A. A. Popov, S. Yang, and L. Dunsch, Endohedral fullerenes, Chem. Rev. **113**, 5989 (2013).

[36] N. A. Romero, J. Kim, and R. M. Martin, Electronic structures and superconductivity of endohedrally doped C_{28} solids from first principles, Phys. Rev. B **76**, 205405 (2007).

[37] J. Li and R. Wu, Two-dimensional multifunctional materials from endohedral fullerenes, Phys. Rev. B **103**, 115417 (2021).

[38] H. Arribart, B. Sapoval, O. Gorochov, and N. LeNagard, Fast ion transport at room temperature in the mixed conductor Cu_3VS_4, Solid State Commun. **26**, 435 (1978).

[39] G. Kresse and J. Furthmüller, Efficiency of ab-initio total energy calculations for metals and semiconductors using a plane-wave basis set, Comput. Mater. Sci. **6**, 15 (1996).

[40] J. P. Perdew, K. Burke, and M. Ernzerhof, Generalized Gradient Approximation Made Simple, Phys. Rev. Lett. **77**, 3865 (1996).

[41] S. L. Dudarev, G. A. Botton, S. Y. Savrasov, C. J. Humphreys, and A. P. Sutton, Electron-energy-loss spectra and the structural stability of nickel oxide: An LSDA + U study, Phys. Rev. B **57**, 1505 (1998).

[42] P. E. Blöchl, Projector augmented-wave method, Phys. Rev. B **50**, 17953 (1994).

[43] H. J. Monkhorst and J. D. Pack, Special points for Brillouin-zone integrations, Phys. Rev. B **13**, 5188 (1976).

[44] M. Brandbyge, J.-L. Mozos, P. Ordejón, J. Taylor, and K. Stokbro, Density-functional method for nonequilibrium electron transport, Phys. Rev. B **65**, 165401 (2002).

[45] J. Taylor, H. Guo, and J. Wang, Ab initio modeling of quantum transport properties of molecular electronic devices, Phys. Rev. B **63**, 245407 (2001).

[46] See the Supplemental Material at http://link.aps.org/supplemental/10.1103/PhysRevApplied.19.054045 for the band structures of isolated MCu_3X_4 and Li-MCu_3X_4, nudged elastic band simulations of H/Li/Na/K in MCu_3X_4, structural parameters of H-MCu_3X_4, phonon spectra of MCu_3X_4 with inserting different atoms, charge transfer in Li-MCu_3X_4, ferromagnetic order and antiferromagnetic order of Li-VCu_3X_4, and the electron structures of the partial filling states for inserting Li into VCu_3S_4.

[47] G. Henkelman, B. P. Uberuaga, and H. Jónsson, A climbing image nudged elastic band method for finding saddle

points and minimum energy paths, J. Chem. Phys. **113**, 9901 (2000).

[48] H. Wang, F. Fan, S. Zhu, and H. Wu, Doping enhanced ferromagnetism and induced half-metallicity in CrI_3 monolayer, Europhys. Lett. **114**, 47001 (2016).

[49] G. Henkelman, A. Arnaldsson, and H. Jónsson, A fast and robust algorithm for Bader decomposition of charge density, Comput. Mater. Sci. **36**, 354 (2006).

[50] L. Li, M. Wang, Y. Zhou, Y. Zhang, F. Zhang, Y. Wu, Y. Wang, Y. Lyu, N. Lu, G. Wang, *et al.*, Manipulating the insulator-metal transition through tip-induced hydrogenation, Nat. Mater. **21**, 1246 (2022).

[51] X. Liu, A. P. Pyatakov, and W. Ren, Magnetoelectric Coupling in Multiferroic Bilayer VS_2, Phys. Rev. Lett. **125**, 247601 (2020).

[52] Y. Zhao, J. Zhang, S. Yuan, and Z. Chen, Nonvolatile electrical control and heterointerface-induced half-metallicity of 2D ferromagnets, Adv. Funct. Mater. **29**, 1901420 (2019).

[53] W. Wang, Y. Gang, Z. Hu, Z. Yan, W. Li, Y. Li, Q.-F. Gu, Z. Wang, S.-L. Chou, H.-K. Liu, *et al.*, Reversible structural evolution of sodium-rich Rhombohedral Prussian Blue for sodium-ion batteries, Nat. Commun. **11**, 980 (2020).